Experimental and Numerical Analysis of Aerodynamic Interaction between Wing and Propeller

A. Savino, L. Menini, L. Riccobene, D. Grassi, A. Zanotti
Politecnico di Milano, Dipartimento di Scienze e Tecnologie Aerospaziali,
via La Masa 34, 20156, Milan, Italy

ABSTRACT

This work aims to investigate the aerodynamic interaction of a of a typical wing-mounted propulsion system representative of a typical eVTOL geometry. The study combines experimental campaigns with a numerical model to extend test results and develop a comprehensive model for exploring configurations with multiple propellers, typical of new eVTOL and distributed propulsion aircraft designs. The experimental data and numerical simulations provide insights into the aerodynamic interactions between wings and propellers, crucial for optimizing the performance and efficiency of such configurations in various flight conditions. The findings contribute to advancing the understanding and design capabilities necessary for future developments in distributed propulsion aircraft technologies.

NOMENCLATURE

R = propeller radius [m]
D = propeller diameter [m]
V_∞ = freestream speed [$\mathrm{m\,s^{-1}}$]
ρ = freestream air density [$\mathrm{kg\,m^{-3}}$]
n = rotational speed [rev/s]
J = advance ratio $V_\infty/(2nR)$ [-]
θ = propeller collective angle at 75% of R [deg]
L = lift force [N]
l = sectional lift force [$\mathrm{N\,m^{-1}}$]
D = drag force [N]
C_L = lift coefficient $= L/(0.5\rho V_\infty bc)$ [-] [-]
C_l = sectional lift coefficient $= l/(0.5\rho V_\infty c)$ [-] [-]
C_D = drag coefficient $= D/(0.5\rho V_\infty bc)$ [-]
L = propeller thrust [N]
P = propeller power [W]
C_T = thrust coefficient $= T/(\rho\pi D^4 n^2)$ [-]
C_P = power coefficient $= P/(\rho\pi D^5 n^3)$ [-]
α = angle of attack [deg]
b = wing span [m]
c = wing chord [m]
c_b = blade chord [m]
y/b = adimensional span coordinate [-]
a = speed of sound [$\mathrm{m\,s^{-1}}$]
N = sectional blade normal force [$\mathrm{N\,m^{-1}}$]
M^2C_n = blade sectional normal force coefficient $= N/(0.5\rho a^2 c_b)$ [-]
u = axial velocity component [$\mathrm{m\,s^{-1}}$]
w = swirl velocity component [$\mathrm{m\,s^{-1}}$]
ψ = blade azimuthal angle [deg]

Copyright Statement.
The authors confirm that they, and/or their company or organization, hold copyright on all of the original material included in this paper. The authors also confirm that they have obtained permission, from the copyright holder of any third-party material included in this paper, to publish it as part of their paper. The authors confirm that they give permission, or have obtained permission from the copy-right holder of this paper, for the publication and distribution of this paper as part of the ERF proceedings or as individual offprints from the proceedings and for inclusion in a freely accessible web-based repository.

INTRODUCTION

The emerging concept of Urban Air Mobility is driving new solutions to enhance and transform current urban transportation systems. Within this context, eVTOLs are at the forefront, offering benefits such as cost and time savings, reduced noise emissions, and lower environmental impact. These electric Vertical Take-Off and Landing (eVTOL) aircraft have the potential to revolutionize urban transportation by combining the vertical take-off and landing capabilities of helicopters with the efficient cruising abilities of airplanes. Typical eVTOL designs utilize Distributed Electric Propulsion (DEP) technology, which replaces traditional single-engine configurations with multiple smaller electric propellers distributed across the wings or fuselage (Refs. 1–3). Various promising eVTOL concepts are being developed by renowned aeronautical companies such as Airbus, Archer, and Vertical, among others. However, this advanced design highlights the complex phenomena of wing-propeller aerodynamic interaction, which can affect aircraft performance and stability, as well as noise emissions and power consumption.

For instance, using Distributed Electric Propulsion alongside a boom configuration highlights the significant issue of wing-propeller aerodynamic interaction. Therefore, this study will focus on evaluating these interactions. The research will examine the effects of variables such as angle of attack, advance ratio, rotational direction, and the longitudinal offset of the propellers on the performance of both the wing and the propellers.

This study builds on previous research by the same authors in collaboration with Archer Aviation (Ref. 4), which involved wind tunnel testing of full-scale eVTOL components from the Maker aircraft, specifically a wing section with a boom-mounted propeller. That work was notable for its unique experimental setup, thanks to the availability of actual eVTOL components, and provided valuable insights into wing-propeller interactions in eVTOL scenarios. However, due to confidentiality restrictions on the geometries used, only a limited amount of data was published.

In contrast, this study presents a comprehensive series of wind tunnel tests on a scaled wing-propeller system with an open geometry. The goal was to generate a detailed and accessible experimental database for investigating key parameters of eVTOL flight conditions, such as cruising and the final transition phase. The research specifically focuses on the effects of aerodynamic interactions between the propeller and wing by varying the angle of attack, advance ratio, and boom length. Various measurement techniques were employed, including global system and propeller load measurements, wing pressure measurements, and Particle Image Velocimetry (PIV) surveys in the propeller wake. The experimental investigation is comprehensively detailed in (Ref. 5). This study, on the other hand, focuses on developing, validating, and applying the corresponding numerical model to extend and build upon the results for future configurations to be tested.

EXPERIMENTAL SET UP

The experimental activity was performed at the *S. De Ponte* wind tunnel of Politecnico di Milano. The closed-loop wind tunnel has a 1 m × 1.5 m test section and can reach a maximum speed of 55 m s^{-1} with a turbulence level lower than 0.1%. The total cumulative electric power is approximately 100*kW* and it has installed different instruments and sensors for a precise identification of the environmental conditions inside the test chamber: static temperature, absolute pressure, differential pressure and humidity are constantly acquired.

Model

The wing model was made by a NACA 23015 airfoil with a chord of 300 mm and an untapered span of 930 mm. The model was manufactured using an internal aluminium structure made by four ribs and two spars and an external cover made by thermoplastic resin.

The propeller is a three-bladed configuration hub equipped with VarioProp 12C blades, thus resulting in a propeller disk diameter equal to 300 mm. A 65 mm diameter aluminium spinner was screwed on the propeller hub and a polycarbonate nacelle with 270 mm length is aimed to shield the driving system and the load cell. The propeller model geometry is available thanks to a 3D scanning of the blades. The system was driven by a Scorpion brushless motor (5.3 kW continuous power) with shaft connected directly to propeller hub. The motor was powered by an external PWM-controlled electronic speed controller. A custom software developed in Labview was used to keep controlled the propeller at the desired rotational speed. A maximum fluctuation below 1% of the target rotational speed of the propeller was found during the wind tunnel tests.

An internal aluminium frame, see Fig. 1(a), was designed to support the propeller driving system and a bi-axial strain gauge load cell. The propeller model was equipped with a Hall-effect sensor that was mounted on the metallic plate below the motor. The Hall-effect sensor was used during the tests to provide the 1/rev signal for the measurement of propeller rotational speed and to trigger the phase-locked PIV measurements.

The propeller model is attached to the wing by means of an outer steel plate resembling the rib shape and a 30 mm × 30 mm squared *Bosch*© aluminium profile, as shown in Fig. 1(a). A cylindrical nylon cover made by 3D printing technique was used as a boom to shield the internal wing-propeller connection structure (see Fig. 1(b)). This set up allowed to perform tests with propeller disk at different distances with respect to the wing's leading edge by varying the length of the connecting *Bosch*© profile, thus resembling eVTOL configurations with different boom length. In particular, the axis of rotation of propeller blades is aligned with wing airfoil chord.

The wing-propeller model was mounted inside the wind tunnel test section by means of a steel shaft attached at wing basement rib enabling the variation of the system angle of attack around 25% airfoil chord axis. A 5 mm gap was left between the wing basement rib and test section floor. The wing-propeller model mounted inside the wind tunnel is shown in Fig. 2.

Measurements set up

Loads measurements set up The supporting steel shaft was connected to an external six-component strain gauge balance mounted on a heavy basement placed below the wind tunnel floor. This balance allowed the measurement of the global aerodynamic forces and moments of the modular system. The balance was calibrated in-house at the Aerodynamics Laboratory of Politecnico di Milano. Loading range

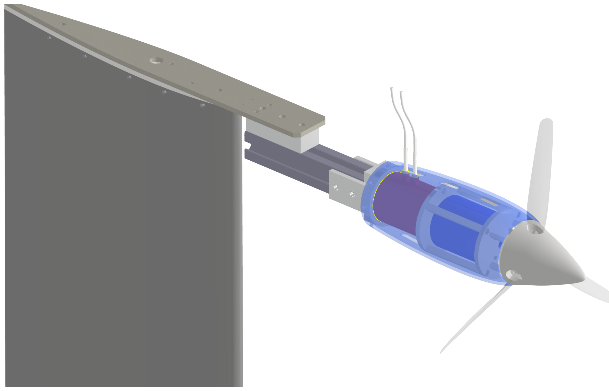

(a)

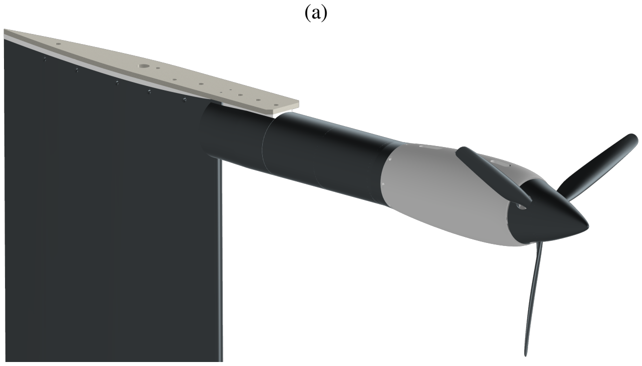

(b)

Figure 1: Layout of the wing-propeller model.

Figure 2: Wing-propeller model mounted inside the wind tunnel test section.

and accuracy of the balance can be found in (Refs. 6, 7). A Futek MBA500 strain gauge bi-axial load cell embedded in the propeller internal metallic structure was used to measure propeller thrust and torque as reported in Fig. 1(a). This load cell has a F.S. range of ±222 N for thrust and of ±5.7 N m for torque (non-linearity ±0.25% R.O., non-repeatability ±0.05% R.O.). Load cells signals were acquired by a National Instrument c-DAQ system equipped with strain/bridge NI 9237 modules. Loads signals of the balances were sampled at 2.5 kHz and averaged over 10 seconds of acquisition time. Each test point was measured four times and results averaged.

Pressure measurements setup Static pressure measurements were performed over 6 airfoil sections along the wing span each equipped with 21 pressure taps, for an overall amount of 126 measurement points. The position of the pressure taps sections expressed as fraction of the propeller R with respect to the hub rotation axis are $0.4R$, $1R$, $2R$, $3.8R$, and $4.9R$. Pressure signals were acquired simultaneously to loads measurements by means of five 32-ports ESP-32HD-DTC pressure scanners and a DTC Initium system at a sampling frequency of $50Hz$.

PIV set up Two-components PIV surveys were performed. The investigated region is shown in Fig. 3.

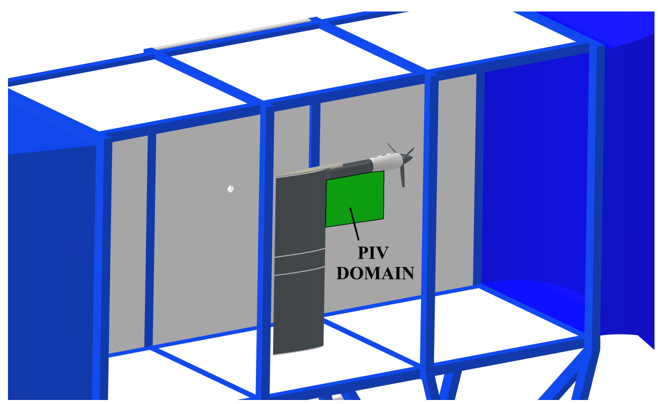

Figure 3: Layout of the PIV setup.

A Quantel Evergreen Nd:Yag double-pulse laser with an output energy of 200 mJ and wavelength of 532 nm was positioned under the floor of wind tunnel test section to generate a laser sheet aligned with the longitudinal $x-y$ mid-span plane by means of a 90° optic mirror. A double-shutter ILA.PIV.sCMOS camera with a 16 bit 2560×2160 pixels array was mounted on an external metallic structure around the test section. This set up allowed an investigation area in the region between the wing leading edge and the propeller boom/nacelle junction with dimensions of 373 mm × 314 mm. A particle generator (PIVpart30 by PIVTEC) equipped with Laskin atomizer nozzles was used to fill wind tunnel test section with seeding. The seeding particles consisted of small dimethyl sebacate droplets with a diameter in the range of 1–2 μm. Free-run and phase-locked 2C PIV measurements respectively over 400 and 250 image pairs were performed for each test configuration considered during the wind tunnel campaign. Image pairs analysis was performed using PIVview 3C software developed by PIVTEC. Post-processing made use of the multi-grid interrogation method (Ref. 8) starting from a 128 pixels $\times$ 128 pixels to a 16 pixels $\times$ 16 pixels interrogation window with effective 50% overlap. This methodology results in a spatial resolution between adjacent measurement points less than 2 mm.

NUMERICAL MODEL

The numerical activity was conducted using the a mid-fidelity aerodynamic code DUST (Ref. 9). DUST is available as open-source software under the MIT license (https://www.dust.polimi.it/) and it relies on an integral boundary element formulation and a vortex particle model for wakes (Refs. 10, 11). It implements a time-stepping algorithm, sequentially solving Morino-like problems for the potential velocity field, nonlinear problems for lifting lines, and updating the rotational velocity field by integrating the Lagrangian dynamical equations of wake particles. The code incorporates various classical aerodynamic elements, such as lifting lines, vortex lattices, non-linear vortex lattices, and surface panels, enabling different fidelity levels in the model.

The DUST numerical model of the wing-propeller system was built using different aerodynamic elements. Figure 4 illustrates the DUST aerodynamic mesh of the considered model.

The wing was modeled as a vortex lattice component while for the nacelle/boom surface panels (SP) were employed. The propeller blades were modeled as lifting lines (LL). Lifting lines elements should comprise a single vortex line representing the circulation introduced by a lifting surface, whose intensity is obtained from the tabulated aerodynamic data of the airfoil section they should represent. The blade geometry used to build the numerical model of the propeller was digitally created by means of a 3D scanning of the blade model. In particular, CAD software was used to generate the blade geometry from the surfaces provided by the scanning system. The maximum difference between the reconstructed blade CAD geometry and the 3D scanned surfaces was below 0.1 mm.

A total number of 12 sections were extracted along the span direction. For each section, the airfoil geometry was extracted and the distribution of twist, chord, sweep, and dihedral was derived along the blade radial coordinate (r). Table 1 reports the airfoil, chord, and twist distribution obtained. Known airfoils were assigned to each section by similarity with the extracted ones.

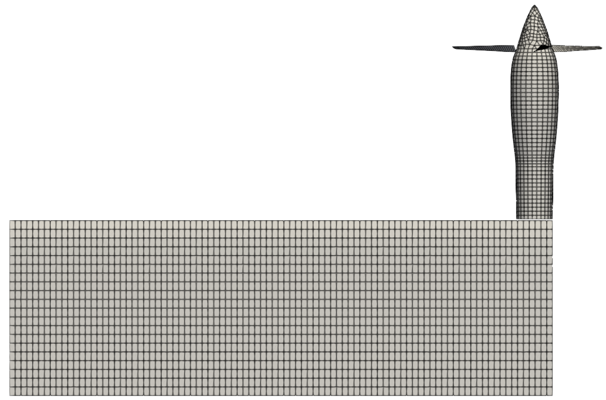

(a) Wing-propeller complete model.

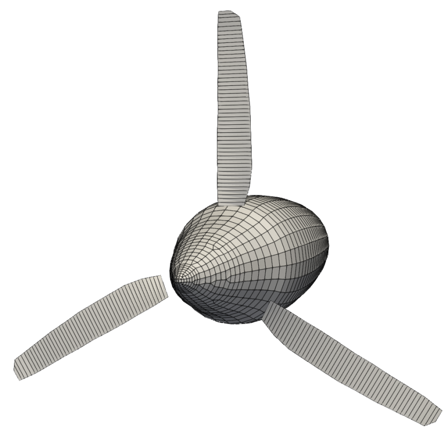

(b) Isolated propeller model.

Figure 4: Numerical DUST model surface mesh.

r/R	chord [m]	twist [deg]	Airfoil
0.24	15.6	24.8	GOE-570
0.32	19.0	15.0	GOE-421
0.39	20.3	9.8	GOE-421
0.47	20.3	6.6	GOE-421
0.55	19.9	4.0	GOE-222
0.62	19.3	2.2	MH-112
0.70	18.5	0.78	GOE-675
0.77	17.5	-0.33	GOE-412
0.85	16.3	-1.07	NACA-4412
0.92	14.9	-1.57	GOE-564
0.97	13.2	-1.40	MH-23
1.00	7.3	-1.24	MH-23

Table 1: Airfoils sections, chord and twist distributions along blade span.

The sectional tabulated aerodynamic coefficients were calculated by XFOIL simulations (Ref. 12) in the angle of attack range before stall. The Viterna method (Ref. 13) was used to calculate the post-stall behavior of the sectional aerodynamic load's coefficients in the range between $\pm 180°$ of the angle of attack.

For each of the three blades the model has a total of 50 elements in a spanwise direction. In order to accurately reproduce the whole experimental propeller model geometry, the spinner-nacelle surface was included in the mesh. In particular, 1212 surface panel elements were used to model the spinner-nacelle geometry. The layout of the isolated propeller mesh built for DUST simulations is shown in Fig. 4(b).Some additional elements were introduced to model the boom part that extends the propeller nacelle to the leading edge of the wing. The wing is discretized into 20 chordwise elements and 100 spanwise elements based on a preliminary convergence study. The choice was made considering the convergence on the lift load while ensuring the most efficient model from a computational cost perspective.

RESULTS

The results section is divided into three parts. In the first part, the focus is on the integral loads provided by experimental balance measurements. This phase evaluates the effects of boom length, propeller rotation direction, angle of attack, and advance ratio. Experimental measurements are compared with the numerical model results in terms of polar data and percentage variations in loads to assess the model's ability to capture the effects observed experimentally. The second part takes into account the sectional loads distribution, both on wing and on propeller's blade exploiting the numerical model. These results clearly show how the aerodynamic interactions act on the loads' distribution. In the third part, an insight on the flowfields is made comparing the PIV measurements with the solution computed numerically.

An overview of the test conditions and parameters for the aerodynamic performance measurements is reported in Tab. 2.

J	V_∞ $[m/s]$	RPM	θ_{out} $[deg]$	θ_{in} $[deg]$
0.50	17.6	7050	20.5	22
0.75	26.4	7050	20.5	22

Table 2: Summary of test conditions and parameters for performance experimental measurements.

Regarding the propeller's direction of rotation, *inboard-up* is defined as the case where the blades, when rotating, move in front of the wing from bottom to top, that is, from the lower side to the upper side of the wing, generating an upwash on the wing. The opposite case is defined as *outboard-up*, where the blades, passing in front of the wing, create a downwash.

The choice to use two different pitch angle of the blades evaluated at 75% span θ for the inboard-up and outboard-up propeller configuration was driven by the difficulty of setting the exact same angle between the two, given that changing the configuration involves changing the blades and remounting them on the hub. For correlation purposes, the pitch angle of the numerical model's propeller is set to match that of the experimental model. Afterward, θ_{out} is set to 22° to distinctly emphasize the influence of the rotational direction.

Integral Loads

First, the lift coefficient measured for the entire system is considered for two advance ratios J in order to highlight the effect of the propeller rotation direction and the effect of the boom length. Figure 5 shows the lift coefficient as a function of the angle of attack α compared to the isolated wing case for the inboard-up and outboard-up propeller configurations considering the short boom configuration.

In the outboard-up regime, the complete setup in the lowest advance ratio ($J = 0.50$) is the only condition that exhibits benefits in terms of lift coefficient for angles of attack above 8°, with an increase in the lift curve slope and in the measured $C_{L_{max}}$. Indeed the maximum lift coefficient increases of about $+7\%$ with respect to the isolated wing. In the other cruise speed conditions, the degradation effect is observable as a down shift on the coefficient without any alterations on the slopes. Outboard-up rotation leads to swirl enhancement and downwash effect: the effective angle of attack of the spanwise wing region washed by the propeller slipstream is reduced. At the highest thrust condition the raise in dynamic pressure can counterbalance the increase in swirl and the subsequent reduction in the effective angle of attack at medium-to-high tilt angle. Then, in all advance ratios, an increase on the incidence angle can reduce the detrimental effect due to propeller-wing interaction. When model is tilted at positive angles of attack, this twisted condition modifies and reduces the effective impinging dynamic pressure and effective swirl component provided by the propeller's wake and thus, the differences in lift coefficient between complete-model and isolated wing are reduced too.

From these results, it is concluded that for $J = 0.75$, the effect of the interaction becomes less evident, whereas for $J = 0.5$, the interaction is well marked and the difference between inboard-up and outboard-up can be appreciated. Therefore, for the condition corresponding to $J = 0.5$, the effect of lengthening the boom is evaluated by comparing the short and long boom configurations, as shown in Fig. 6. For long boom configuration, as expected, the interactional effect decreases, as wing airfoils experience a reduced variation of the local axial velocity due to the higher longitudinal offset of the propeller disk. The long boom lift curve is slightly downward shifted with respect to the short boom one. Based on these results, the long boom configuration is not further investigated in this study.

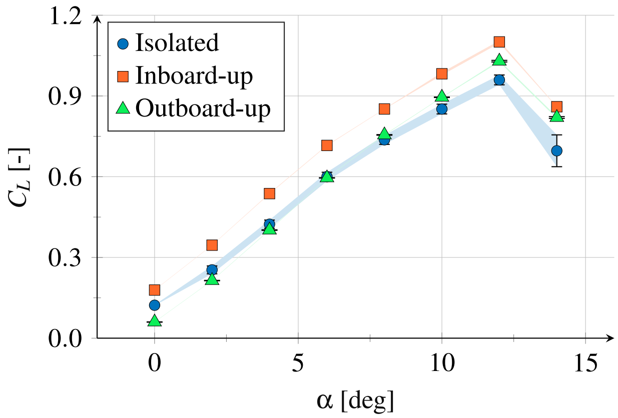

(a) $J = 0.5$.

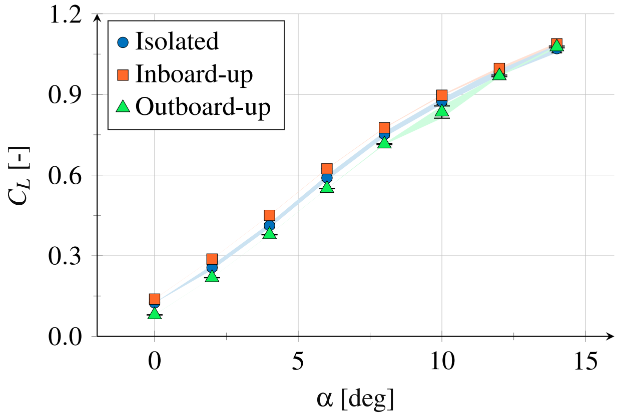

(b) $J = 0.75$.

Figure 5: Measured lift coefficient as function of angle of attack for the inboard-up and outboard-up configuration compared to the isolated case for different adavance ratios J. The colored band represents the error as one σ confidence level.

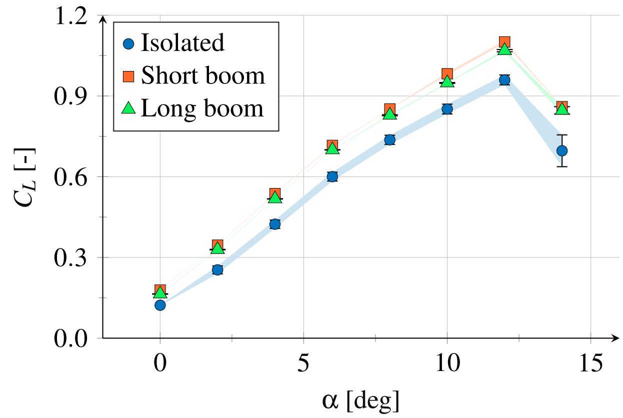

(a) Inboard up.

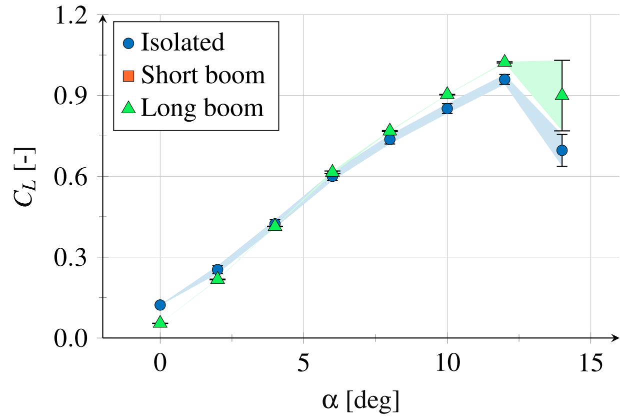

(b) Outboard up.

Figure 6: Measured lift coefficient as function of angle of attack for the inboard-up and outboard-up configuration compared to the isolated case for different boom's length at $J = 0.5$. The colored band represents the error as one σ confidence level.

In order to correlate the numerical model, the first step is to verify that the isolated propeller is aligned in terms of loads with the experimental measurements. This is necessary to ensure that the effects produced by it on the wing are as consistent as possible. Thrust and power coefficients are compared with varying advance ratio J. The results for the case with a pitch angle of $\theta = 22°$ are shown in Fig. 7. The numerical model is the one depicted in Fig. 4(b). The DUST model of this propeller has been widely used and extensively validated in the past under different flight conditions, including more complex non-axisymmetric conditions, (Ref. 14).

In general, the correlation is good for both coefficients throughout the entire considered envelope.

The entire wing-propeller system is now considered in order to verify the numerical model's ability to capture the main effects related to the interactional aerodynamics involved in such a case and described previously. The comparison is made by considering the total load of the entire system ex-

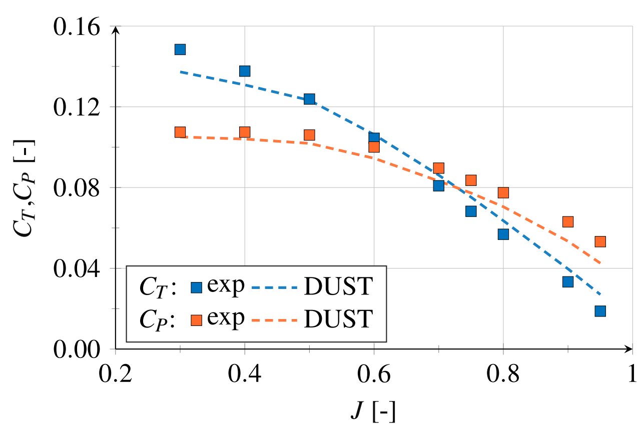

Figure 7: Isolated rotor thrust and power coefficient ($\theta = 22°$).

pressed in terms of the $C_L - C_D$ polar curve. Fig. 8 shows the results obtained considering the 'short' boom configuration for the two advance ratios considered during the experimental tests for the cases of isolated wing, inboard-up, and outboard-up. For both flight conditions, the numerical model aligns with the experimental measurements in terms of the global polar curve within the region before stall occurs. In the regime corresponding to $J = 0.75$, the absolute value of the global drag coefficient is much lower than the condition at $J = 0.5$ primarily because the measurement includes the contribution of the propeller thrust, which is lower at higher forward speeds. In both cases, it is evident that the inboard-up propeller configuration corresponds to greater system efficiency, although it should be considered that between the inboard-up and outboard-up configurations, the propeller has a different collective pitch angle.

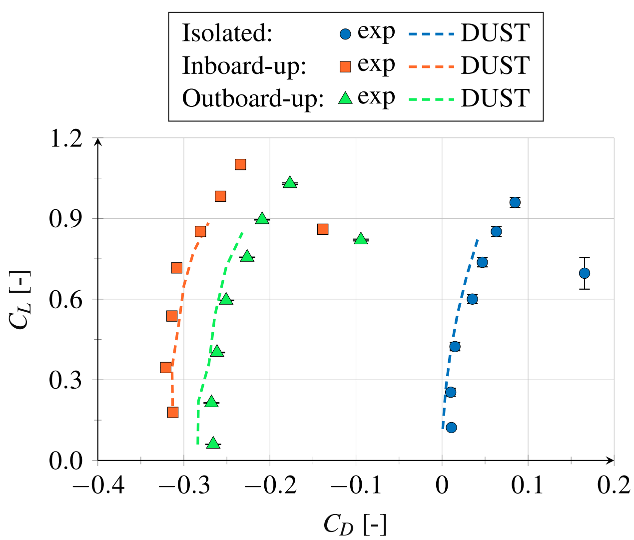

(a) $J = 0.5$.

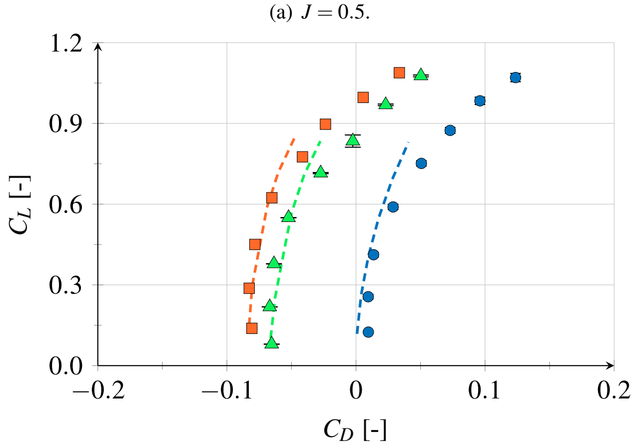

(b) $J = 0.75$.

Figure 8: Complete system polar for the inboard-up and outboard-up configuration compared to the isolated case. Comparison between experimental and numerical results.

A better quantitative understanding can be obtained by observing the percentage variation of the lift coefficient of the entire system. In Fig. 9, the ΔC_L produced by the presence of the propeller in the inboard-up configuration is shown compared to the case of the isolated wing, obtained from both experimental measurements and numerical modeling.

In the case of inboard up propeller, the positive increase in the overall lift coefficient tends to decrease as the angle of attack α increases, but it always remains positive. As already highlighted by the polar curves in Fig. 8, the interaction is less significant for a higher advance ratio, approximately halving the ΔC_L.

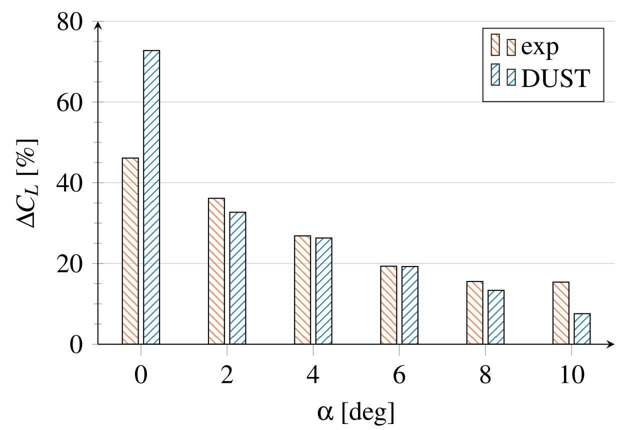

(a) $J = 0.5$.

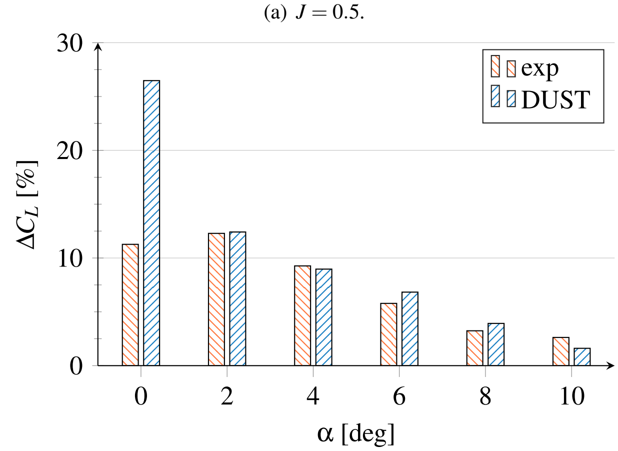

(b) $J = 0.75$.

Figure 9: Percentage change in the lift coefficient ΔC_L for the inboard-up configuration.

In Fig. 10, the same results for the outboard-up configuration are shown. In this case, the increments ΔC_L are smaller in absolute value. Here, since the two effects related to the interaction, namely the increase in dynamic pressure and the downwash angle on the wing, counteract each other, there is an increment that can change sign. Specifically, at low angles of attack, the effect of downwash induced by the wake of the propeller on the wing dominates, resulting in a decrease in the lift coefficient compared to the isolated wing. At higher angles, however, the effect of increased dynamic pressure becomes predominant, resulting in an overall slight increase in lift.

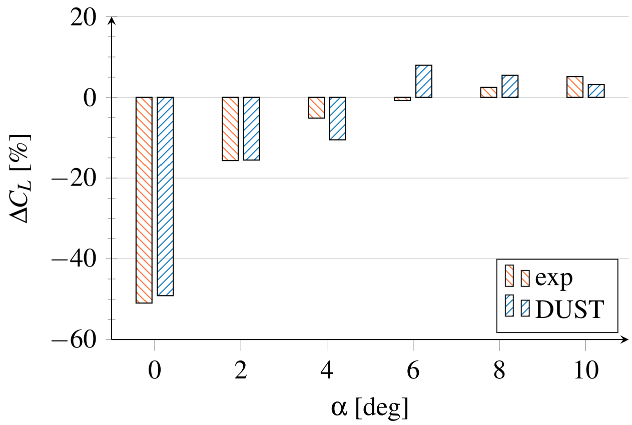

(a) $J = 0.5$.

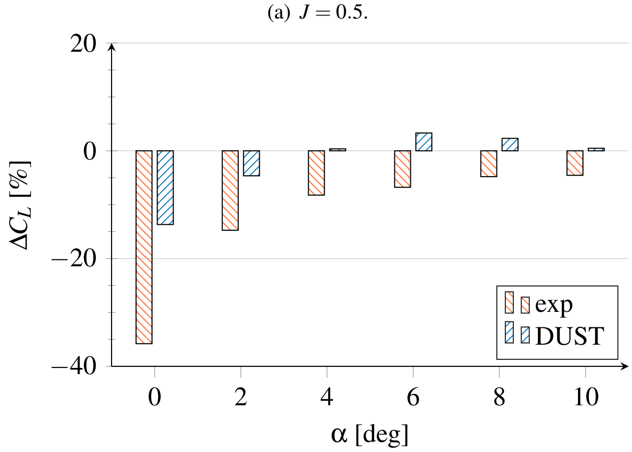

(b) $J = 0.75$.

Figure 10: Percentage change in the lift coefficient ΔC_L for the outboard configuration.

The numerical model seems capable of capturing this type of interactional phenomenology. The greatest discrepancy between the numerical model and experimental measurements occurs in the case of outboard-up propeller at $J = 0.75$, where the esperiment always detects a reduction in performance for all tested angles of incidence. However, these differences could be attributed to the fact that with DUST's medium fidelity approach, the loads of the bluff bodies are not well captured, such as the contribution of the boom, which becomes increasingly significant as α increases.

In order to perform a consistent comparison between the inboard-up and outboard-up configurations, the numerical model is used to impose the same propeller collective angle θ equal to 22°.

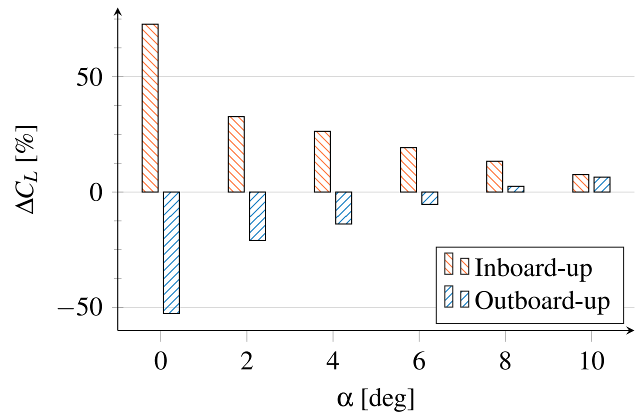

Figure 11: DUST percentage change in the lift coefficient ΔC_L for the inboard-up and outboard-up configuration at $J = 0.5$.

Fig. 11 shows the ΔC_L obtained at constant propeller collective angle for the condition of $J = 0.5$. Even at the same θ, the effect of interaction on the overall lift coefficient is greater in the inboard-up configuration. In order to isolate more effectively the propeller's effect on the wing, only the integral load of the wing itself is extracted. Fig. 12 shows the $CL-\alpha$ curves of the isolated wing, inboard-up and outboard-up configurations for $J = 0.5$. From these, it is evident that the inboard-up case generates a higher wing load, especially at low angles of incidence. The opposite holds true for the outboard-up case. Additionally, the interaction introduces a change in the slope of the curve, resulting in a reduction in the inboard-up case and an increase in the outboard-up case. Finally, Fig. 13 presents a comparison in terms of polar curve considering only the load of the wing. For the inboard-up case, the polar curve shows that besides an increase in the wing's lift coefficient, there is also a reduction in its drag coefficient. The opposite is true for the outboard-up configuration.

Sectional Loads

To obtain a more detailed understanding of the wing load distribution, the averaged sectional lift coefficient along the wingspan is considered. Experimental values are obtained by integrating the pressure coefficient measured at the six sections of the model equipped with pressure taps. Note that the dimensionless coordinate y/b equals 0 at the root and 1 at the tip where the propeller is positioned. For these results, three angles of attack are considered, $\alpha = 0, 4, 10^\circ$.

As a first step, it is verified that the numerical model aligns with the experimental measurements considering the isolated wing case. Figure 14 shows the comparison considering the condition at $J = 0.5$. Apart from a slight underestimation of the load obtained with DUST, the comparison is considered satisfactory. Note that in the numerical model, an additional

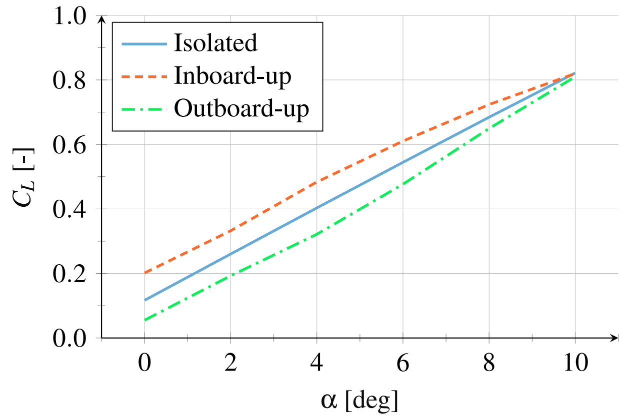

Figure 12: DUST wing lift coefficient as function of angle of attack for the inboard-up and outboard-up configuration compared to the isolated case at $J = 0.5$.

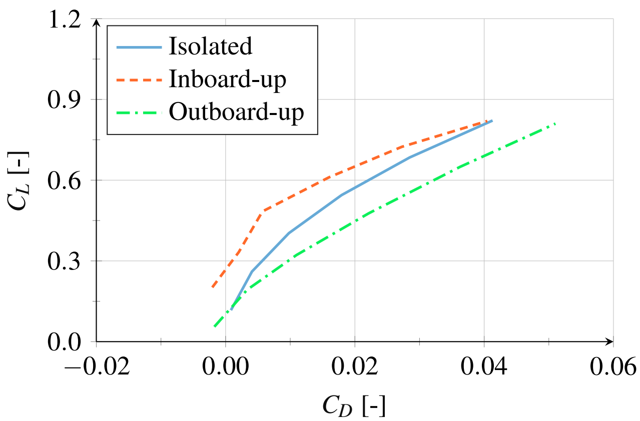

Figure 13: DUST wing polar for the inboard-up and outboard-up configuration compared to the isolated case at $J = 0.5$.

wing segment has been introduced to prevent decay in the root area of the wing, replicating the effect of the wind tunnel wall on the load.

Introducing the presence of the propeller, in Fig. 15 the loads are shown for the inboard-up case, while in Fig. 16 for the outboard-up case. As already highlighted by the integrated loads, for a lower advance ratio J, the interaction becomes more pronounced because the wake of the propeller is more intense compared to the freestream. The numerical model allows for a complete understanding of what happens even in areas where the model does not have pressure taps, enabling the capture of peak loads.

While for the inboard-up configuration in the wing tip area there is always an increase in sectional load, in the case of outboard-up this is not always true. In particular, observing the condition corresponding to $J = 0.5$ in Fig. 16(a), it is noted that for $\alpha = 0°$, in the region starting from $y/b = 0.8$,

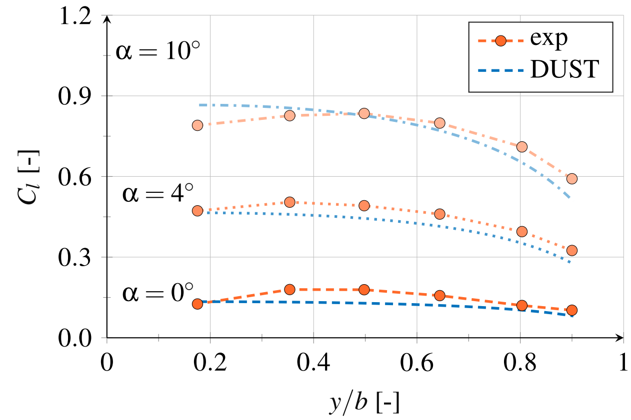

Figure 14: Isolated wing sectional lift coefficient along the wing span ($J = 0.5$).

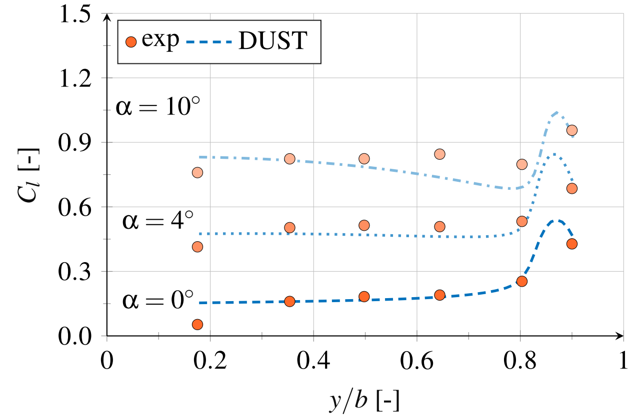

(a) $J = 0.5$.

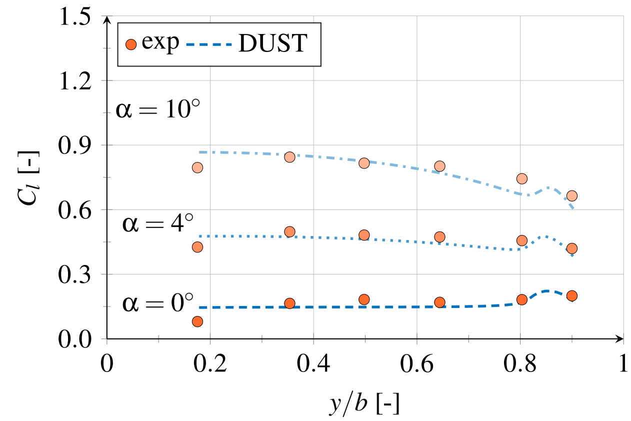

(b) $J = 0.75$.

Figure 15: Inboard configuration: sectional lift coefficient along the wing span.

the sectional C_L decreases, while increasing the angle of attack leads to an increase in load, as clearly visible from the case corresponding to $\alpha = 10°$.

A clearer insight is obtained by directly comparing the sec-

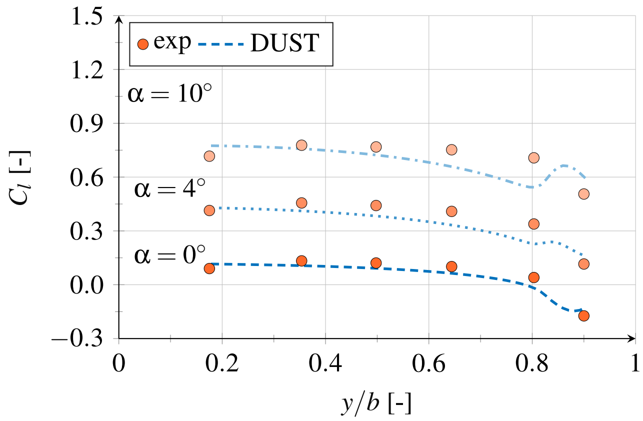

(a) $J = 0.5$.

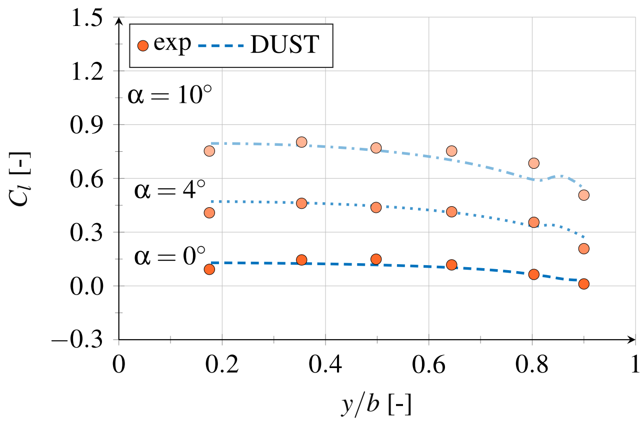

(b) $J = 0.75$.

Figure 16: Outboard configuration: sectional lift coefficient along the wing span.

tional load between isolated wing, inboard-up configuration, and outboard-up configuration considering the same collective propeller angle $\theta = 22°$ as shown for the case of $J = 0.5$ in Fig. 17.

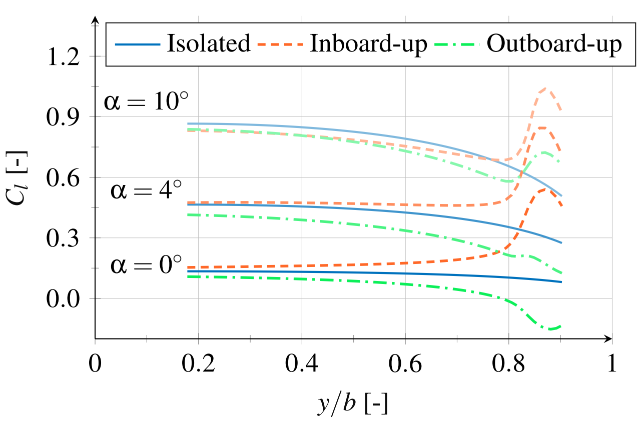

Figure 17: DUST sectional lift coefficient along the wing span ($J = 0.5$).

By obtaining the same type of result in terms of sectional load along the propeller blades, it is possible to get an idea of how the total load of the propeller is distributed across its disk. In particular, Fig. 18 shows a comparison of the contours of the blade non-dimensional normal force ($M^2 c_n$) computed over the last rotor revolution in order to provide a detailed insight into the rotor/wing aerodynamic interaction effect on the local blade airloads.

Considering the case of zero angle of attack, the loads on the propeller disc between the inboard-up and outboard-up configurations are practically identical, as shown in Fig. 18(a) and Fig. 18(b). This is because since the wing generates little load, its induction on the blades is reduced. However, by increasing the angle of attack of the whole system and observing the result obtained for $\alpha = 10°$, differences are noticeable, as shown in Fig. 18(c) and Fig. 18(d). In particular, the load on the disc becomes asymmetrical, showing a region where it increases by approximately 20%. In the inboard-up case, this region occurs approximately for $\psi = 300°$ to $60°$, i.e., after the blade has passed in front of the wing. The effect of increased load manifests with a certain phase delay. A similar discussion can be made for the outboard-up configuration, where the region of increased load on the disc is approximately between $\psi = 60°$ and $180°$. In this case, it seems that the phase delay from the blade passing in front of the wing is less compared to the inboard-up case. The ability to capture this phenomenology in the blade load is an important factor for aeroacoustic evaluations as this phase shift implies directivity in the loading term. The first aeroacoustic applications of the DUST software were presented in (Ref. 15) and future works will also consider a wing-propeller test case.

Flowfields

To thoroughly investigate the physics of the interaction, it is crucial to examine the flow field in the region downstream of the propeller. This area is of particular interest because it is where the effects of the propeller's operation are most apparent and where the interaction between the propeller and the wing behind it originates. Experimental measurements using Particle Image Velocimetry (PIV) are employed to correlate and validate the numerical model. The PIV technique provides detailed insights into the flow characteristics by capturing both average and instantaneous flow fields. By comparing these experimental results with the numerical predictions, we can assess the accuracy and reliability of the numerical model. The average flow field data obtained from PIV measurements reveal the overall patterns and structures of the flow with the relative intensities. In addition to average flow fields, instantaneous flow field data from PIV are crucial for capturing transient phenomena and fluctuations in the flow. These measurements provide a snapshot of the flow at specific moments in time, allowing for a detailed examination of

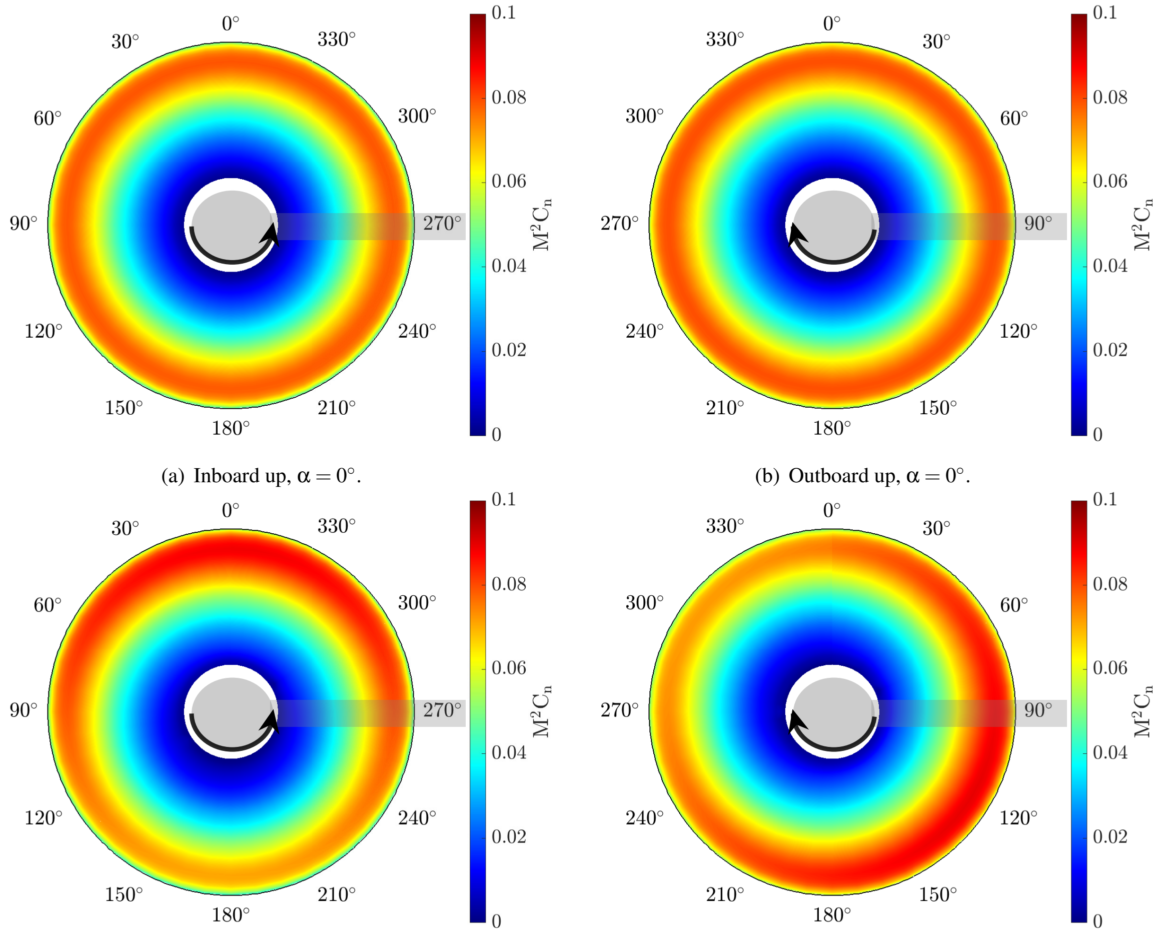

(a) Inboard up, $\alpha = 0°$.

(b) Outboard up, $\alpha = 0°$.

(c) Inboard up, $\alpha = 10°$.

(d) Outboard up, $\alpha = 10°$.

Figure 18: Comparison of the non-dimensional normal force M^2C_n on the proprotor blade, $J = 0.5$.

how the propeller's wake evolves and interacts with the surrounding air. By integrating both average and instantaneous flow field data from PIV with the numerical simulations, we can achieve a comprehensive understanding of the propeller's impact on the downstream flow. This approach ensures that the numerical model not only aligns with the steady-state behavior of the flow but also accurately represents the transient dynamics, leading to a more robust and validated model for predicting propeller performance and interaction effects.

In Fig. 19, the comparison of the time-averaged non-dimensional axial velocity u/V_∞ is shown for the outboard-up configuration at $J = 0.5$ and $J = 0.75$. Axial velocity contours gives information about the average acceleration of the flow within the propeller's wake. Specifically, at the lowest advance ratio $J = 0.5$, the velocity inside the propeller's wake reaches values around 50% higher than the freestream velocity. On the other hand, at the highest advance ratio $J = 0.75$, as shown in Fig. 19(b) and Fig. 19(d), the local flow acceleration provided by the propeller is quite limited because of the lower induced velocity developed by the propeller disk at increasing inflow speed. The numerical results seem to align well with the experimental ones in terms of overall behavior, and especially demonstrate the ability to capture the effect related to the change in advance ratio J.

Exploiting the numerical model, the swirl velocity component can be extracted. In Fig. 20, a comparison of the average swirl velocity w perpendicular to the measurement plane is shown between the inboard-up and outboard-up configurations for an advance ratio $J = 0.5$ and $\alpha = 0°$. Note that a positive sign for the velocity w indicates a velocity directed out of the plane, while a negative sign indicates a velocity directed into the plane. For the inboard-up configuration, as shown in Fig. 20(a), the average swirl velocity component reaches up to approximately 40% of the freestream velocity V_∞ and peaks at 50% near the leading edge of the wing. The same intensities but in the opposite direction are observed for the outboard-up case, as seen in Fig. 20(b).

The phase-locked PIV measurements provided insights into

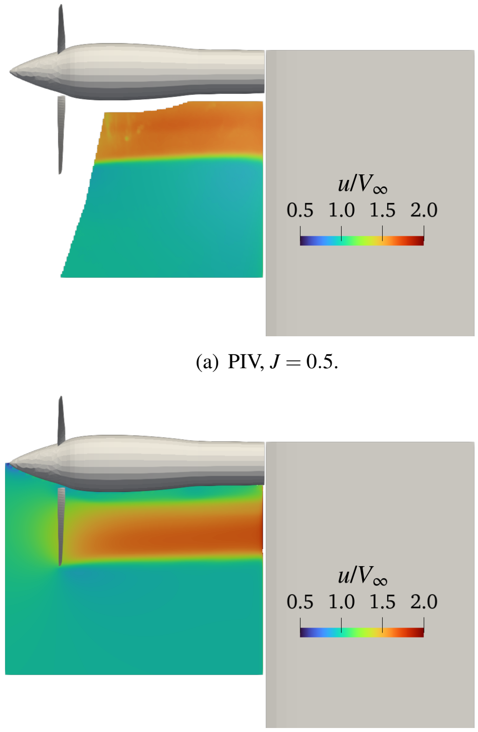

(a) PIV, $J = 0.5$.

(b) PIV, $J = 0.75$.

(c) DUST, $J = 0.5$.

(d) DUST, $J = 0.75$.

Figure 19: Comparison of the time-averaged non-dimensional axial velocity component u at $\alpha = 0^\circ$ in outboard-up configuration at $J = 0.5$ and $J = 0.75$.

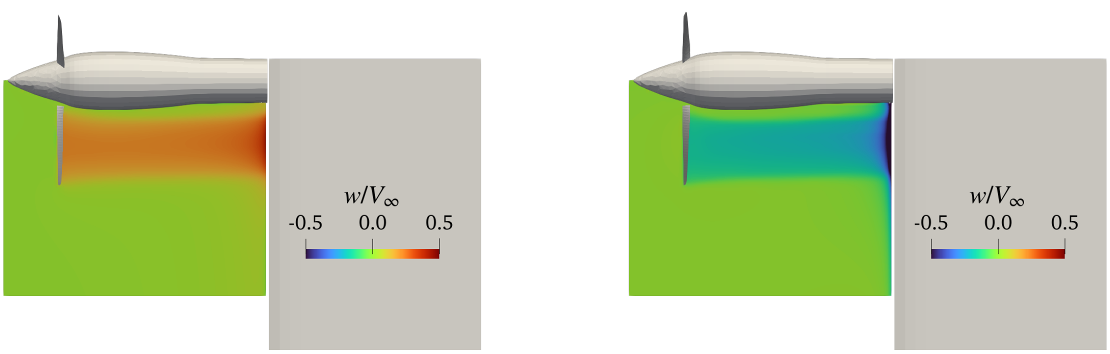

(a) Inboard up.

(b) Outboard up.

Figure 20: DUST comparison of the time-averaged non-dimensional swirl velocity component w at $\alpha = 0^\circ$ and $J = 0.75$.

the evolution of the propeller wake under different flight conditions. The experimental measurements are actually averaged fields considering the fixed phase of the propeller in order to obtain clean measurements. On the other hand, the numerical result is the instantaneous flow field extracted at the desired phase. Figure 21 shows the comparison of the contours of the phase-averaged non-dimensional axial velocity u at $\alpha = 0^\circ$ and blade azimuthal angle $\psi = 0^\circ$ and the two considered advanca ratios J.

From the instantaneous flow field, we can clearly discern the tip vortices generated by the propeller blades. These vortices become notably more intense when the advance ratio is lower. This is because, with a fixed collective pitch, a lower asymptotic velocity V_∞ results in a higher induced velocity from the propeller, thereby increasing its load. Consequently, the strength of the vortices is amplified in such scenarios. From the perspective of numerical correlation, the DUST shows a strong ability to accurately capture both the intensity of these

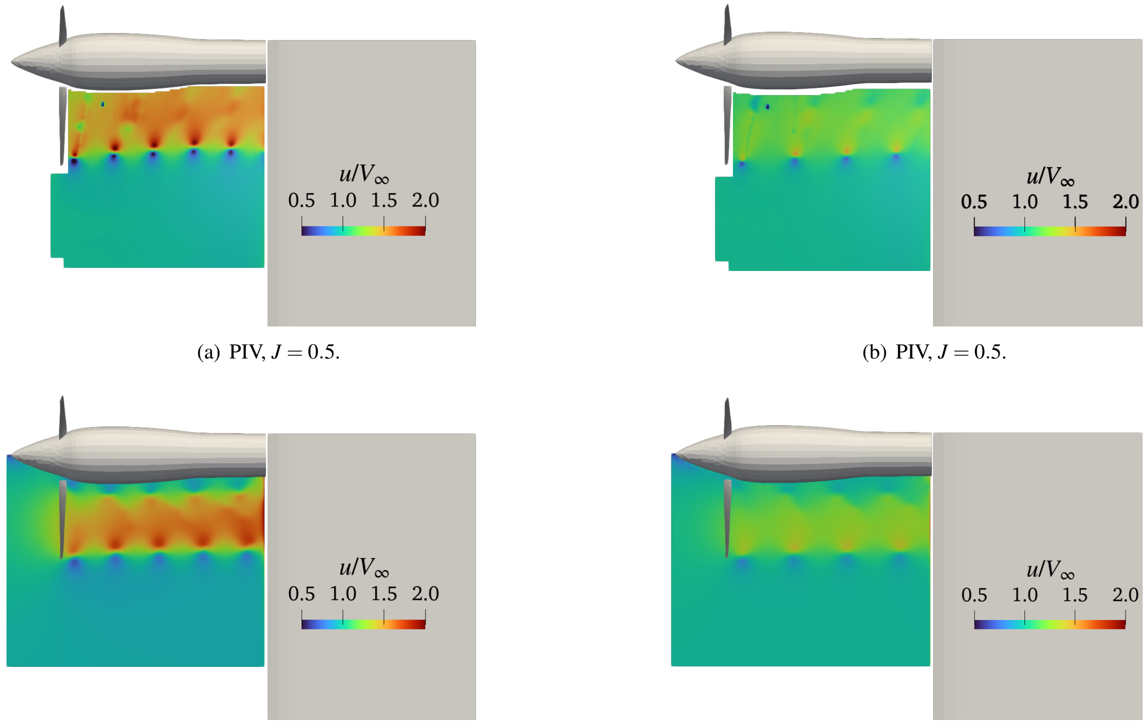

(a) PIV, $J = 0.5$.

(b) PIV, $J = 0.5$.

(c) DUST, $J = 0.75$.

(d) DUST, $J = 0.75$.

Figure 21: Comparison of the instantaneous non-dimensional axial velocity component u at $\alpha = 0^\circ$ in outboard-up configuration at $J = 0.5$ and $J = 0.75$.

vortices and the overall wake phenomena. This is particularly evident in the simulations shown in Fig. 21, where DUST effectively reproduces the vortex positions in both depicted cases. The numerical model aligns well with the observed flow characteristics, demonstrating its reliability in capturing critical aspects of the vortex dynamics and wake structures. In the region near the nacelle wall, the numerical model reveals the presence of vortices released from the blade root. These vortices, however, do not appear in the experimental measurements. The absence of these vortices in the experimental data could be attributed to the fact that Particle Image Velocimetry (PIV) images in that specific area were masked, and hence, detailed measurement information for this region is not available. The presence of these root vortices in the DUST model may be due to the design of the simulation, which includes a gap between the blade and the spinner. This gap can facilitate the formation of vortices at the blade root tip where the flow detaches. Despite this, the intensity of these vortices is relatively lower compared to the tip vortices. This reduced intensity is because the load on the blade root is lower, which is a result of the decreased tangential velocity at this section of the blade. In summary, while the numerical model predicts the presence of blade root vortices, their lower intensity and the lack of corresponding data from experimental measurements due to masking of PIV images make it challenging to fully assess their impact.

CONCLUSIONS

In this work, the aerodynamic interaction in a wing-propeller system installed at the wingtip was investigated. A numerical model was used alongside wind tunnel experiments to understand the main effects of this interaction in a typical eVTOL configuration. Additionally, the study demonstrated the capability of the mid-fidelity software DUST to capture the interaction effects observed in experiments. The use of the numerical model allowed extending the investigation to elements that are difficult to measure experimentally, such as the azimuthal load on the propeller blades or a broader view of the flow field, which is often limited in the experimental setup. This enhanced capability provides a more comprehensive understanding of the aerodynamic behaviors and interactions within the system. For instance, by examining the azimuthal load, researchers can gain insights into the distribution of forces around the propeller blades, which is crucial for optimizing performance and reducing noise. Moreover, the numerical model offers a detailed view of the overall flow field, enabling the identification of complex flow patterns that might be missed in experimental setups due to limitations in measurement techniques or spatial constraints.

However, it's important to note that the numerical model has limitations due to the software formulation. Specifically, it does not model flow separations and does not accurately capture loads on bluff bodies. The inability to model this accurately can affect the reliability of the simulation under certain conditions. Despite these limitations, under typical operational conditions where the aircraft operates in pre-stall regimes, the approach proves to be quite accurate. In pre-stall conditions, the flow remains attached to the surfaces, minimizing the impact of the model's limitations. This accuracy is particularly beneficial when considering the low computational cost of the numerical model. The efficiency of the model allows for the exploration of multiple rotor configurations, which is a common requirement in the development of distributed propulsion systems. Distributed propulsion systems, which involve multiple smaller rotors distributed across the airframe, offer potential benefits in terms of efficiency, noise reduction, and redundancy.

In summary, while the numerical model has some limitations, its ability to extend investigations to difficult-to-measure elements and its accuracy in pre-stall regimes make it a valuable tool. The low computational cost further enhances its utility, enabling extensive exploration of various configurations, which is essential for advancing the design and performance of modern propulsion systems.

REFERENCES

1. Johnson, W., and Silva, C., "NASA concept vehicles and the engineering of advanced air mobility aircraft," *The Aeronautical Journal*, Vol. 126, (1295), Publisher: Cambridge University Press, January 2022, pp. 59–91. DOI: 10.1017/aer.2021.92.

2. Afonso, F., Ferreira, A., Ribeiro, I., Lau, F., and Suleman, A., "On the design of environmentally sustainable aircraft for urban air mobility," *Transportation Research Part D: Transport and Environment*, Vol. 91, February 2021, pp. 102688. DOI: 10.1016/j.trd.2020.102688.

3. Kadhiresan, A. R., and Duffy, M. J., "Conceptual Design and Mission Analysis for eVTOL Urban Air Mobility Flight Vehicle Configurations," *AIAA Aviation 2019 Forum*, AIAA AVIATION Forum, American Institute of Aeronautics and Astronautics, June 2019. DOI: 10.2514/6.2019-2873.

4. Riccobene, L., Grassi, D., Braukmann, J. N., Kerho, M., Droandi, G., and Zanotti, A., "Wind tunnel test of full-scale wing-propeller system of a eVTOL aircraft," *The Aeronautical Journal*, 2023, pp. 1–15.

5. Zanotti, A., Menini, L., Savino, A., Grassi, D., and Riccobene, L., "Experimental investigation of wing-propeller aerodynamic interaction in eVTOL configurations," *Aerospace Science and Technology*, 2024, pp. 109348.

6. Bertagnini, M., *Studio degli effetti aerodinamici indotti dai rotori sull'ala di un convertiplano durante la fase di conversione*, Master's thesis, Politecnico di Milano, 2015.

7. Droandi, G., Gibertini, G., Grassi, D., Campanardi, G., and Liprino, C., "Proprotor–wing aerodynamic interaction in the first stages of conversion from helicopter to aeroplane mode," *Aerospace Science and Technology*, Vol. 58, November 2016, pp. 116–133. DOI: 10.1016/j.ast.2016.08.013.

8. Raffel, M., Willert, C., Wereley, S., and Kompenhans, J., *Particle image velocimetry — a practical guide*, Springer, Berlin, 2007.

9. Tugnoli, M., Montagnani, D., Syal, M., Droandi, G., and Zanotti, A., "Mid-fidelity approach to aerodynamic simulations of unconventional VTOL aircraft configurations," *Aerospace Science and Technology*, Vol. 115, 2021, pp. 106804.

10. Winckelmans, G. S., *Topics in vortex methods for the computation of three-and two-dimensional incompressible unsteady flows*, Ph.D. dissertation, California Institute of Technology, 1989.

11. Cottet, G. H., and Koumoutsakos, P. D., *Vortex methods: theory and practice*, Cambridge University Press, 2000.

12. Drela, M., "XFOIL: An Analysis and Design System for Low Reynolds Number Airfoils," Low Reynolds Number Aerodynamics, edited by T. J. Mueller, 1989.

13. Viterna, L. A., and Janetzke, D. C., "Theoretical and experimental power from large horizontal-axis wind turbines," Technical report, Washington Procurement Operations Office, Washington, DC (United States), September 1982.

14. Zanotti, A., Velo, A., Pepe, C., Savino, A., Grassi, D., and Riccobene, L., "Aerodynamic interaction between tandem propellers in eVTOL transition flight configurations," *Aerospace Science and Technology*, Vol. 147, 2024, pp. 109017.

15. Caccia, F., Abergo, L., Savino, A., Morelli, M., Zhou, B. Y., Gori, G., Zanotti, A., Gibertini, G., Vigevano, L., and Guardone, A., "Multi-fidelity numerical approach to aeroacoustics of tandem propellers in eVTOL airplane mode," AIAA Aviation 2023 Forum, 2023.